Supporting Information

Reversible Red-green Photoluminescence Transformation Induced by Dynamic Coordination Bonds in a Phase-transition Hybrid Crystal

Yu-Xuan Wang[+],[a] Ming-Yu Guo[+],[b] Tong Xie,[a] Lin Chen,[a] De-Xuan Liu,*[a] Wei-Xiong Zhang,[b] and Guo-Ming Wang*[a]

E-mail: gmwang_pub@163.com, dexuan_liu@163.com

Experimental

Synthesis

All chemicals were purchased and used without any further purification: The chemical reagents employed in this study, including 4-morpholinopyridine ($C_9H_{12}N_2O$, 98%), manganese chloride tetrahydrate ($MnCl_2 \cdot 4H_2O$, 98%), hydrochloric acid (HCl, 36-38%) were purchased as commercially available reagent and used without further purification. Crystals of **1** were prepared by slowly evaporating the methanol solution of 4-morpholinopyridine, hydrochloric acid and $MnCl_2 \cdot 4H_2O$ with the stoichiometric ratio of 2:2:1. Colorless crystals were obtained after 5 days.

Thermal analyses

Thermogravimetric analysis (TGA) was performed on TG 209 F3 thermal analyzer from room temperature to 650 ℃ at a heating rate of 10 K min^{-1} under argon atmosphere. DSC analyses were performed from 273 K to 473 K on TA DSC250 thermal analyzer under nitrogen atmosphere with rate of 10 K min^{-1}.

PL and Common characterization

Photoluminescence (PL) and photoluminescence excitation spectra (PLE) measurements were performed with an Edinburgh FS5 spectrofluorimeter. The time-resolved photoluminescence (TRPL) spectra and absolute PL quantum yields were measured by the Edinburgh FLS1000 Steady-State/transient Fluorescence Spectrometer equipped with integrating spheres. Ultraviolet-visible spectra were recorded with a Persee TU-1901 double beam ultraviolet-visible spectrophotometer. The infrared spectra were measured by the Thermo Fisher Nicolet Summit FTIR spectrometer. The Raman spectra were tested by the Thermofisher DXR2 Laser Micro-Raman Spectrometer. The nonlinear optical signal was measured by Mini nots 1064+2100 second-order nonlinear optical test system.

X-ray diffraction crystallography

SCXRD measurements were performed on a Rigaku XtaLAB Synergy DW_Hypix6000 single crystal diffraction (Mo *K*α, λ = 0.71073 Å). Data processing, including cell refinement and data reduction, was carried out with the CrystalClear software (Rigaku). The crystal structures were solved by direct method. The structures were solved and refined with the SHELX program package within the Olex^2 interface.[S1] Refinement was carried out against F^2 using a full-matrix least-squares technique. All non-hydrogen atoms were refined with anisotropic thermal parameters, whereas the hydrogen atoms of organicmolecules were positioned isotropically. The crystal data and structure refinement results at different temperatures for **1** are listed in Table S1. Powder X-ray diffraction (PXRD) data were collected at room temperature in air using Rigaku diffractometer with graphite-monochromated Cu K_α radiation (λ = 1.54184 Å) in the 2θ range of 5°–50°.

Deep Potential Development

Deep Potential Molecular Dynamics (DPMD) leverages machine learning to construct a high-dimensional potential energy surface (PES) that maps atomic structures (lattice parameters, atom types, and coordinates) to their corresponding energies, forces, and virials. This approach enables efficient and accurate MD simulations by replacing computationally expensive quantum mechanical calculations with a deep-learned potential. In this work, the deep-learned potential was developed using the DP-GEN framework,[S2] which combines active learning, first-principles calculations, and neural network training to iteratively refine the potential. The workflow consists of three main stages. (i) Initial Training. An initial dataset was generated from 5% down-sampling short AIMD trajectories in NPT-F ensemble at 600 K, 1 atm, 5 ps with time-step of 1 fs, using CP2K 2023.1 at PBE-D3.[S3-S5] /DZVP-MOLOPT-SR-GTH with the aids of dpdata[S6] and Multiwfn.[S7,S8] The sampling were initiated from the experimental structures of the **1α**, **1β**, and **1β** (200)@H_2O phases with disorder parts properly removed. The DFT settings included a plane-wave cutoff energy

of 800 Ry/60 Ry referring to the convergence benchmarks in our previous work[S9], with gamma-point sampling and a self-consistent field (SCF) convergence threshold of 1×10^{-5}. The initial dataset was used to train deep neural networks with the DeePMD-kit 2.2.9 package.[S10,S11] The structural information were represented as per-atom local environment with cutoff radius of 6.0 Å, smooth radius of 0.5 Å, and maximum neighbour of 160. The architecture employed the DPA1 without attention layers,[S12] featuring an embedding network sized (12, 24, 48) and sub-matrix sized 12, and a fitting network of sizes (160, 160, 160). The training steps were 600000 with learning rate decaying from 10^{-3} to 3×10^{-8} every 3000 steps. (ii) Exploration and Model Deviation. Four models were trained in parallel with different random initialization seeds. The exploration stage was conducted with a short MD using Large-scale Atomic/Molecular Massively Parallel Simulator (LAMMPS),[S13,S14] where new atomic configurations were sampled based on model deviations monitored during the MD. The temperature and pressure covered the range of 300 to 600 K and 0 to 1 bar. (iii) Labeling. Configurations with relative force deviation ranging from 0.5 to 0.75 were labeled using DFT and added to the training dataset, iteratively improving the potential's accuracy. The above procedure finally sampled 8498 frames within 10 iterations. Finally, the accuracy achieved more than 99%. Model compression[S15] was applied to accelerate MD simulations without sacrificing accuracy.

Molecular Dynamics Simulation

DPMD simulations were performed using LAMMPS to investigate the temperature-dependent behavior of the system. A single continuous simulation was carried out with stepwise stage-like targeting to the temperatures of 300 K. The initial structure was constructed by cleaving the (200) surface of **1β**, followed by expanding it into a 2×3×1 supercell and adding an amorphous water layer containing 60 molecules above the surface. The simulations were carried out in the NVT ensemble with a timestep of 1 fs. The temperature and pressure were controlled using a Nosé-Hoover thermostat, with damping times of 0.05 ps. The system was firstly energy-minimized, followed by continuous production runs for 2 ns at each temperature, during which the

trajectory data were saved every 1000 steps.

Post processing was carried out with the aids of MDAnalysis[S16] to characterize the torsion of $[MnCl_4]^{2-}$ with or without water existence. For each recorded frame at time ti, the distance between each Mn atom and surrounding Cl atoms was computed as

$$d_{\mathrm{Mn-Cl}} = |\mathbf{r}_{\mathrm{Mn}} - \mathbf{r}_{Cl}| \quad (1)$$

where $\mathbf{r}_{\mathrm{Mn}}$ and $\mathbf{r}_{\mathrm{Cl}}$ denote the instantaneous position vectors of the Mn and Cl atoms, respectively. Periodic boundary conditions were applied using the minimum image convention to ensure the shortest interatomic distance within the simulation cell. Only Cl atoms satisfying $d_{\mathrm{Mn–Cl}} < 3.0$ Å were considered as bonded neighbors. For each Mn atom with two or more neighboring Cl atoms, the metal–halide–halide bond angle $\theta_{\mathrm{Cl–Mn–Cl}}$ was calculated according to

$$cos(\Theta_{Cl-Mn-\mathrm{Cl}}) = \frac{\mathbf{v}_1 - \mathbf{v}_2}{|\mathbf{v}_1||\mathbf{v}_2|} \quad (2)$$

where $\mathbf{v}_1 = \mathbf{r}_{\mathrm{Cl1}} - \mathbf{r}_{\mathrm{Mn}}$ and $\mathbf{v}_2 = \mathbf{r}_{\mathrm{Cl2}} - \mathbf{r}_{\mathrm{Mn}}$ are the bond vectors from the Mn center to two neighboring Cl atoms. The average Mn–Cl distance $\langle d_{\mathrm{Mn–Cl}} \rangle$ and average Cl–Mn–Cl angle $\langle \theta_{\mathrm{Cl–Mn–Cl}} \rangle$ were evaluated at each sampled frame, and their time evolution was recorded throughout the trajectory.

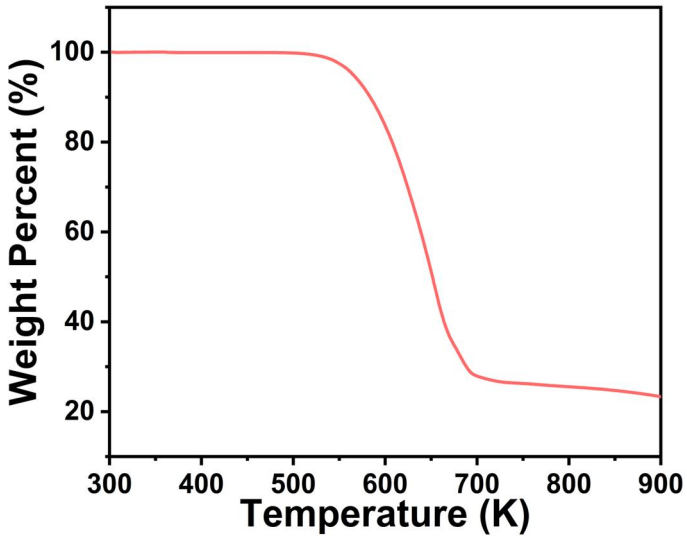

Figure S1. TGA curve for **1**.

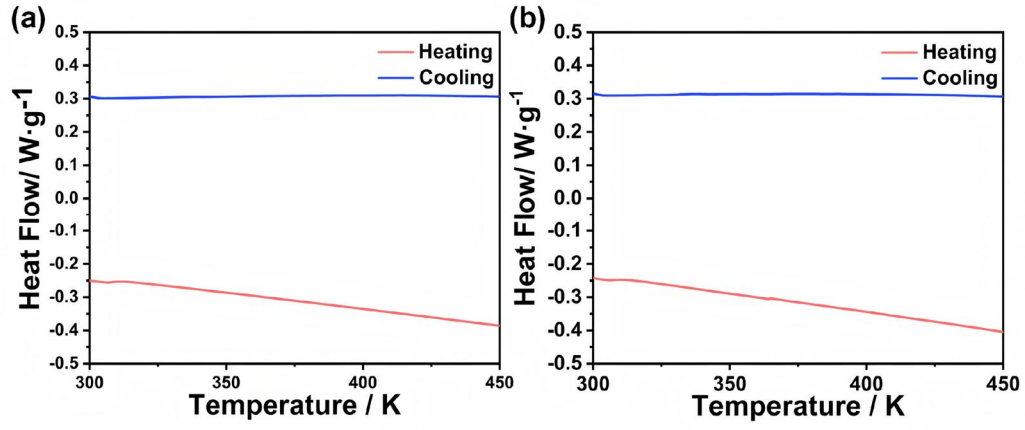

Figure S2. The (a) second and (c) third cycle of DSC measurements for **1**, which reveals no thermal anomaly.

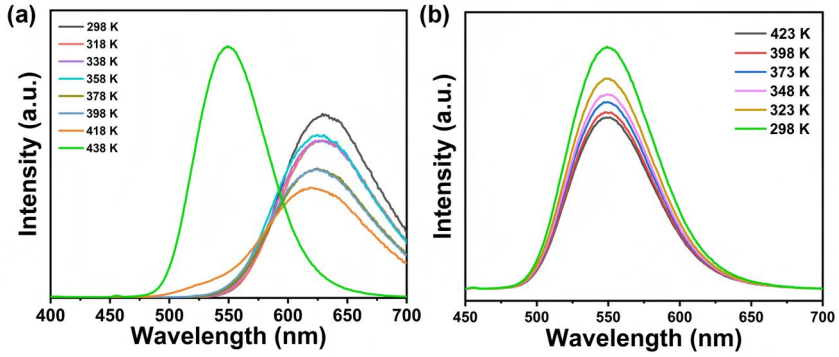

Figure S3. Temperature-dependent PL spectra of **1** during (a) heating and (b) cooling progress.

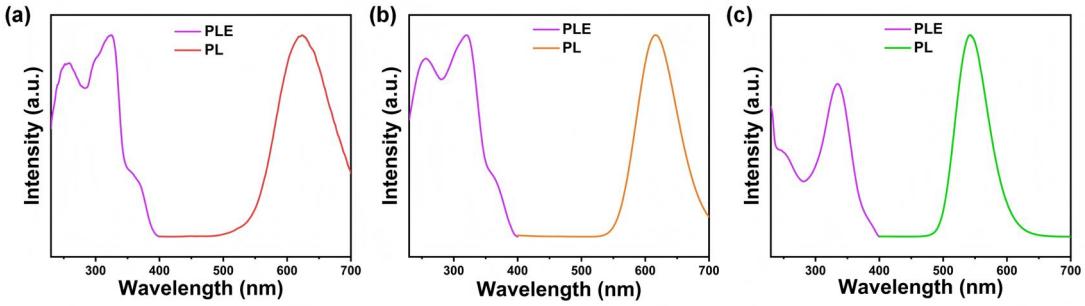

Figure. S4. PL and PLE spectra for (a) **1α,** (b) **1TS** and (c) **1β**.

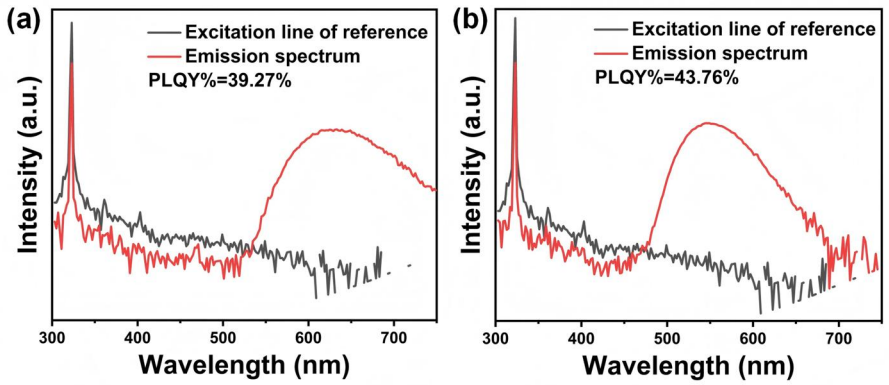

Figure. S5. The PLQYs of (a) **1α** and (b) **1β**.

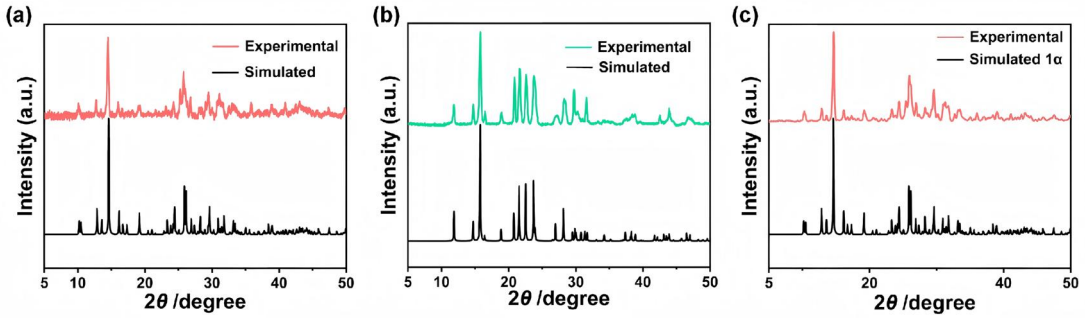

Figure S6. The simulated and experimental PXRD patterns of (a) **1α** and (b) **1β**. (c) The PXRD pattern of the sample restored from **1β** to **1α**.

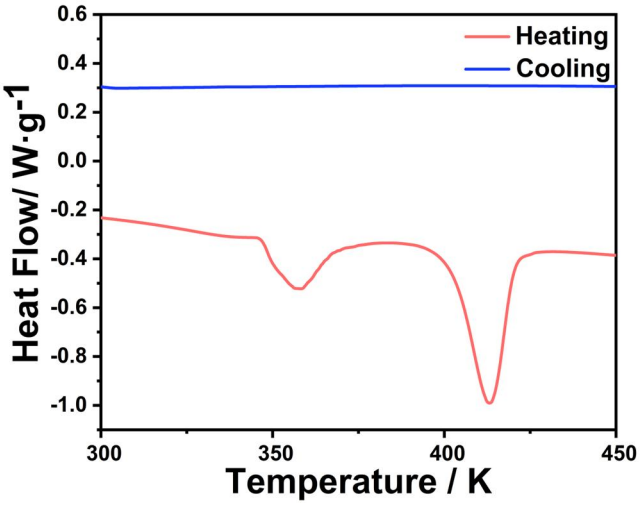

Figure S7. The first cycle of DSC measurement of the sample restored from **1β** to **1α**.

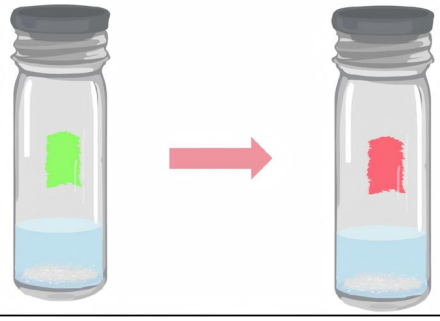

Standard salt solution	Humidity
H_2O	100%
$ZnSO_4$	90%
$(NH_4)SO_4$	81%
CuCl	68%
NaBr	58%
$Ca(NO_3)_2$	50%
$Zn(NO_3)_2$	42%
$CaCl_2$	31%
CH_3COOK	20%
$ZnCl_2$	10%

Figure S8. Standard saturated salt solutions in vials to control the humidity.

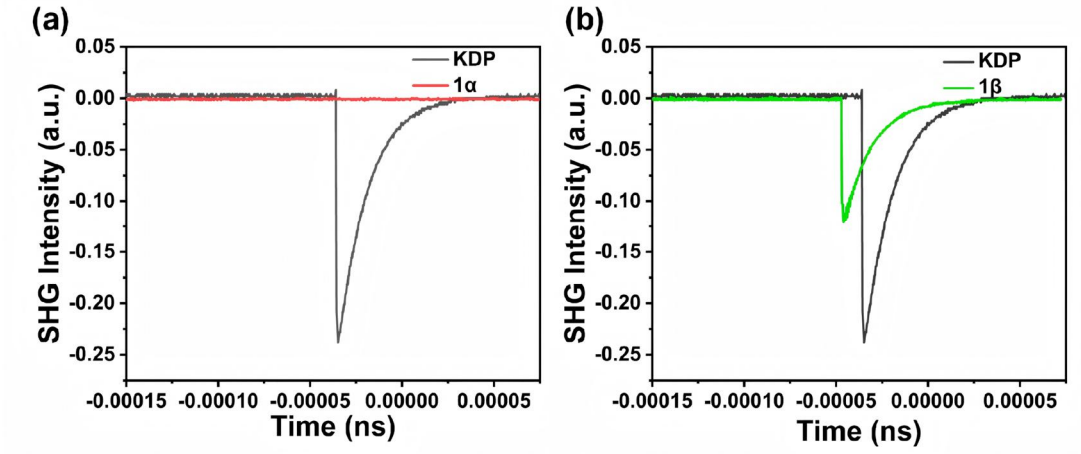

Figure S9. SHG signals of (a) **1α** and (b) **1β** with KDP.

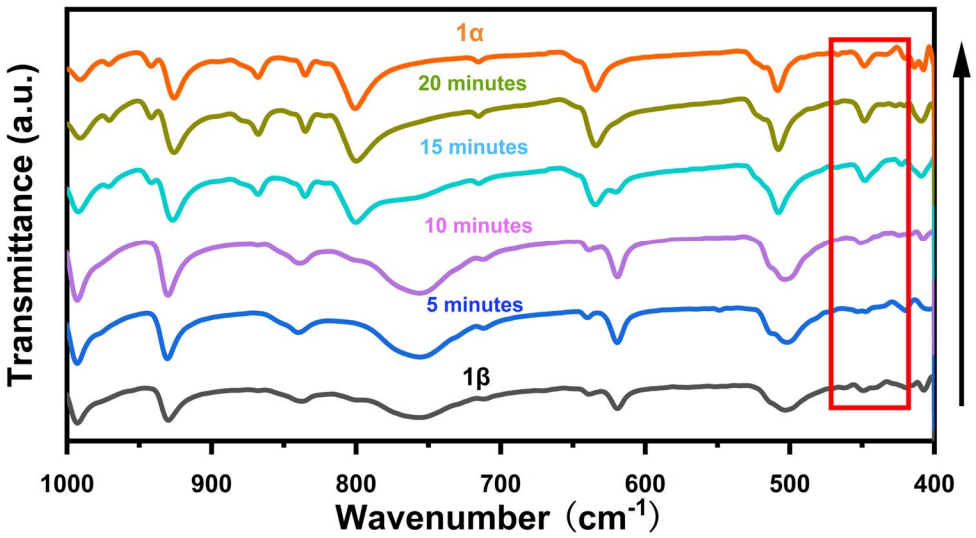

Figure S10. FTIR spectra during the **1β** to **1α** process.

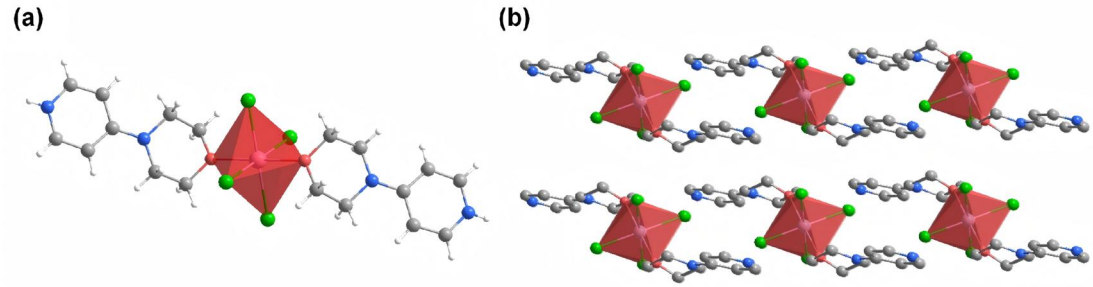

Figure S11. The (a) coordination structure and (b) packing view of the single crystal returned from **1β** to **1α**.

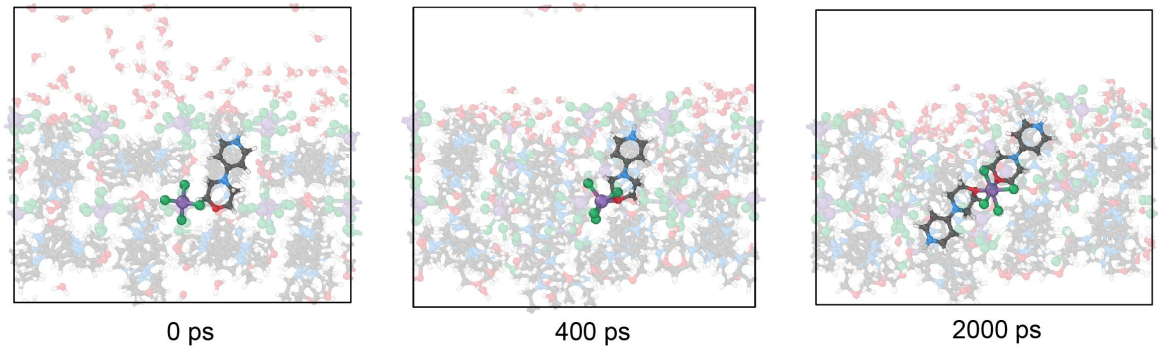

Figure S12. Formation of Mn–O bonds between $C_9H_{13}N_2O^+$ cations and Mn^{2+} during the molecular dynamics process.

Table S1. Single crystal X-ray diffraction data of **1α**, **1β** and **1TS** crystals.

Compound	$(C_9H_{13}N_2O)_2MnCl_4$		
Formula weight	527.17	527.17	527.17
Temperature/K	297.89(10)	377.96(17)	422.99(19)
Phase	**1α**	**1TS**	**1β**
Crystal system	triclinic	triclinic	tetragonal
Space group	$P\bar{1}$	$P\bar{1}$	$I\bar{4}2d$
a/Å	7.3089(4)	7.3414(5)	17.1951(12)
b/Å	8.6750(5)	8.6898(6)	17.1951(12)
c/Å	8.9616(7)	8.9857(6)	8.3920(10)
α/°	89.030(5)	89.023(5)	90
β/°	70.310(6)	70.399(6)	90
γ/°	87.782(4)	87.801(5)	90
Volume/Å^3	534.58(6)	539.62(6)	2481.3(5)
Z	1	1	4
ρ_{calc} g/cm3	1.638	1.622	1.411
μ/mm^{-1}	1.141	1.130	0.983
Goodness − of − fit on F ^{2}	1.112	1.162	1.000
Final R indexes [I>=2σ (I)]	R_1 = 0.0502, wR_2 = 0.1337	R_1 = 0.1094, wR_2 = 0.3387	R_1 = 0.0610, wR_2 = 0.1893
Final R indexes [all data]	R_1 = 0.0576, wR_2 = 0.1374	R_1 = 0.1194, wR_2 = 0.3426	R_1 = 0.1306, wR_2 = 0.2445
CCDC number.	2499777	2499778	2499779

[a] $R_1=\Sigma||F_o| - |F_c||/\Sigma|F_o|$. [b] $wR_2 =[\Sigma w(F_o^2 - F_c^2)^2/\Sigma w(F_o^2)^2]^{1/2}$

Table S2. Single crystal X-ray diffraction data of the crystal returned from **1β** to **1α**.

Compound	$(C_9H_{13}N_2O)_2MnCl_4$
Formula weight	534.61
Temperature/K	298.1(8)
Crystal system	triclinic
Space group	$P\bar{1}$
a/Å	7.3127(9)
b/Å	8.6726(10)
c/Å	8.9574(9)
α/°	89.030(9)
β/°	70.344(10)
γ/°	87.892(9)
Volume/Å^3	534.61(11)
Z	1
ρ_{calc} g/cm^3	1.631
μ/mm^{-1}	1.141
Goodness − of − fit on F ^{2}	1.208

Final *R* indexes [I>=2σ (I)]	R_1 = 0.0592, wR_2 = 0.1673
Final *R* indexes [all data]	R_1 = 0.0665, wR_2 = 0.1695

Table S3. Selected bond lengths (Å) and bond angles (°) for **1α**.

Atom	Length/Å	Atom	Angle/°
Mn1–Cl1	2.520(2)	Cl1–Mn1–Cl1^1	180.0
Mn1–Cl1^1	2.520(2)	Cl1^1–Mn1–Cl2^1	89.2(1)
Mn1–Cl2^1	2.531(1)	Cl1^1–Mn1–Cl2	90.7(0)
Mn1–Cl2	2.531(1)	Cl1–Mn1–Cl2^1	90.7(0)
Mn1–O1^1	2.271(2)	Cl1–Mn1–Cl2	89.2(0)
Mn1–O1	2.271(2)	Cl2–Mn1–Cl2^1	180.0
O1–C7	1.426(4)	O1^1–Mn1–Cl1	92.5(1)
O1–C8	1.428(4)	O1–Mn1–Cl1	87.4(1)
N2–C3	1.356(4)	O1^1–Mn1–Cl1^1	87.4(1)
N2–C9	1.471(4)	O1–Mn1–Cl1^1	92.5(1)
N2–C6	1.462(4)	O1–Mn1–Cl2	86.9(1)
N1–C5	1.344(5)	O1^1–Mn1–Cl2	93.0(1)
N1–C1	1.330(5)	O1^1–Mn1–Cl2^1	86.9(1)
C3–C4	1.412(4)	O1–Mn1–Cl2^1	93.0(1)
C3–C2	1.421(4)	O1–Mn1–O1^1	180.0
C4–C5	1.359(4)	C7–O1–Mn1	124.3(2)
C2–C1	1.364(5)	C7–O1–C8	109.5(2)
C7–C6	1.508(5)	C8–O1–Mn1	124.6(2)
C9–C8	1.502(4)	C3–N2–C9	119.8(3)
		C3–N2–C6	120.2(3)
		C6–N2–C9	116.4(2)
		C1–N1–C5	120.8(3)
		N2–C3–C4	121.8(3)
		N2–C3–C2	121.7(3)
		C4–C3–C2	116.5(3)
		C5–C4–C3	120.3(3)
		C1–C2–C3	119.6(3)
		O1–C7–C6	110.8(3)
		N1–C5–C4	121.1(3)
		N2–C9–C8	112.2(3)
		N1–C1–C2	121.6(3)
		O1–C8–C9	111.2(3)
		N2–C6–C7	112.4(3)

Table S4. Selected bond lengths (Å) and bond angles (°) for **1TS**.

Atom	Length/Å	Atom	Angle/°
Mn1–Cl1^1	2.523(2)	Cl1–Mn1 –Cl1^1	180.0
Mn1–Cl1	2.523(2)	Cl1–Mn1 –Cl2^1	90.8(1)

Mn1–Cl2[1]	2.532(2)	Cl1–Mn1 –Cl2	89.1(1)
Mn1–Cl2	2.532(2)	Cl1[1]–Mn1 –Cl2[1]	89.1(1)
Mn1–O1	2.288(7)	Cl1[1]–Mn1 –Cl2	90.8(1)
Mn1–O1[1]	2.288(7)	Cl2–Mn1 –Cl2[1]	180.0(1)
O1–C1	1.435(12)	O1[1]–Mn1 –Cl1	87.6(2)
O1–C4	1.416(12)	O1[1] –Mn1 –Cl1[1]	92.4(2)
N1–C5	1.352(11)	O1 –Mn1 –Cl1[1]	87.6(2)
N1–C3	1.464(12)	O1 –Mn1 –Cl1	92.4(2)
N1–C2	1.462(12)	O1 –Mn1 –Cl2[1]	87.4(2)
N2–C7	1.350(14)	O1[1] –Mn1 –Cl2[1]	92.6(2)
N2–C8	1.350(14)	O1 –Mn1 –Cl2	92.6(2)
C9–C5	1.404(13)	O1[1] –Mn1 –Cl2	87.4(2)
C9–C8	1.347(14)	O1[1] –Mn1 –O1	180.0
C5–C6	1.412(13)	C1 –O1 –Mn1	124.2(6)
C7–C6	1.360(15)	C4 –O1 –Mn1	124.6(7)
C1–C2	1.503(14)	C4 –O1 –C1	110.1(8)
C3–C4	1.496(14)	C5 –N1 –C3	119.7(8)
		C5 –N1 –C2	120.1(8)
		C2 –N1 –C3	116.7(8)
		C8 –N2 –C7	120.7(9)
		C8 –C9 –C5	122.3(10)
		N1 –C5 –C9	122.9(9)
		N1 –C5 –C6	121.8(9)
		C9 –C5 –C6	115.3(8)
		N2 –C7 –C6	120.5(10)
		O1 –C1 –C2	110.3(8)
		C7 –C6 –C5	120.9(10)
		C9 –C8 –N2	120.0(10)
		N1–C3 –C4	113.0(9)
		O1 –C4 –C3	111.1(9)
		N1 –C2 –C1	112.6(10)

Table S5. Selected bond lengths (Å) and bond angles (°) for **1β**.

Atom	Length/Å	Atom	Angle/°
Mn1–Cl1	2.374(2)	Cl1–Mn1–Cl1[1]	105.8(1)
Mn1–Cl1[1]	2.374(2)	Cl1[2]–Mn1–Cl1[3]	105.8(1)
Mn1–Cl1[2]	2.374(2)	Cl1[1]–Mn1–Cl1[2]	117.1(1)
Mn1–Cl1[3]	2.374(2)	Cl1–Mn1–Cl1[2]	105.8(1)
N2–C3	1.294(17)	Cl1[1]–Mn1–Cl1[3]	105.8(1)
N2–C4[4]	1.411(12)	Cl1–Mn1–Cl1[3]	117.1(1)
N2–C4	1.411(12)	C3–N2–C4[4]	124.5(8)
N1–C1[4]	1.283(16)	C3–N2–C4	124.5(8)
N1–C1	1.283(16)	C4[4]–N2–C4	111.1(16)

C3–C2	1.364(11)	C1–N1–C1[4]	120.3(18)
C3–C2[4]	1.364(11)	N2–C3–C2[4]	122.9(6)
C2–C1	1.299(17)	N2–C3–C2	122.9(6)
O1–C5	1.205(18)	C2–C3–C24	114.3(13)
O1–C5[4]	1.204(18)	C1–C2–C3	121.4(12)
		C5[4]–O1–C5	122(2)
		N1–C1–C2	121.3(15)
		O1–C5–C4	122.8(16)
		N2–C4–C5	120.0(13)

References

(S1) O. V. Dolomanov, L. J. Bourhis, R. J. Gildea, J. A. K. Howard, H. Puschmann, OLEX2: a complete structure solution, refinement and analysis program, *J. Appl. Cryst.*, **2009,** *42* (2), 339-341.

(S2) Y. Z. Zhang, H. D. Wang, W. J. Chen, J. Z. Zeng, L. F. Zhang, H. Wang, W. N. E, DP-GEN: A concurrent learning platform for the generation of reliable deep learning based potential energy models, *Comput. Phys. Commun*., **2020**, *253*, 107206.

(S3) J. P. Perdew, K. Burke, M. Ernzerhof, Generalized Gradient Approximation Made Simple, *Phys. Rev. Lett*., **1996**, *77*, 3865-3868.

(S4) S. Grimme, J. Antony, S. Ehrlich, H. Krieg, A consistent and accurate ab initio parametrization of density functional dispersion correction (DFT-D) for the 94 elements H-Pu, *J. Chem. Phys*., **2010**, *132*, 154104.

(S5) S. Grimme, S. Ehrlich, L. Goerigk, Effect of the damping function in dispersion corrected density functional theory, *J. Comput. Chem*., **2011**, *32*, 1456-1465.

(S6) J. Z. Zeng, X. L. Peng, Y. B. Zhuang, H. D. Wang, F. B. Yuan, D. Zhang, R. X. Liu, Y. Z. Wang, P. Tuo, Y. Z. Zhang, Y. X. Chen, Y. F. Li, C. T. Nguyen, J. M. Huang, A. Y. Peng, M. Rynik, W. H. Xu, Z. Z. Zhang, X. Y. Zhou, T. Chen, J. H. Fan, W. R. Jiang, B.

W. Li, D. N. Li, H. X. Li, W. S. Liang, R. L. Liao, L. P. Liu, C. X. Luo, L. G. Ward, K. W. Wan, J. J. Wang, P. Xiang, C. Q. Zhang, J. C. Zhang, R. Zhou, J. X. Zhu, L. F. Zhang, H. Wang, dpdata: A Scalable Python Toolkit for Atomistic Machine Learning Data Sets, *J. Chem. Inf. Model*., **2025**. DOI:10.1021/acs.jcim.5c01767

(S7) T. Lu, F. W. Chen, Multiwfn: A multifunctional wavefunction analyzer, *J. Comput. Chem.*, **2012**, *33*, 580-592.

(S8) T. Lu, A comprehensive electron wavefunction analysis toolbox for chemists, Multiwfn, *J. Chem. Phys*., **2024**, *161*, 082503.

(S9) M. Y. Guo, Y. F. Yan, P. Chen, W. X. Zhang, DeepEMs-25: a deep-learning potential to decipher kinetic tug-of-war dictating thermal stability in energetic materials, *npj Comput. Mater*., **2025**, *11*, 246.

(S10) H. Wang, L. F. Zhang, J. Q. Han, W. N. E, DeePMD-kit: A deep learning package for many-body potential energy representation and molecular dynamics, *Comput. Phys. Commun*., **2018**, *228*, 178-184.

(S11) J. Z. Zeng, D. Zhang, D. H. Lu, P. H. Mo, Z. Y. Li, Y. X. Chen, M. Rynik, L. A. Huang, Z. Y. Li, S.C. Shi, Y. Z. Wang, H. T. Ye, P. Tuo, J. B. Yang, Y. Ding, Y. F. Li, D. Tisi, Q. Y. Zeng, H. Bao, Y. Xia, J. M. Huang, K. Muraoka, Y. B. Wang, J. H. Chang, F. B. Yuan, S. L. Bore, C. Cai, Y. N. Lin, B. Wang, J. Y. Xu, J. X. Zhu, C. X. Luo, Y. Z. Zhang, Rhys E. A. Goodall, Wenshuo Liang, Anurag Kumar Singh, Sikai Yao, Jingchao Zhang, R. Wentzcovitch, J. Q. Han, J. Liu, W. L. Jia, D. M. York, W. N. E, R. Car, L. F. Zhang, H. Wang, DeePMD-kit v2: A software package for deep potential models, *J. Chem. Phys*., **2023**, *159*, 054801.

(S12) D. Zhang, H. R. Bi, F. Z. Dai, W. R. Jiang, X. Z. J. Liu, L. F. Zhang, H. Wang, Pretraining of attention-based deep learning potential model for molecular simulation, *npj Comput. Mater*., **2024**, *10*, 94.

(S13) S. Plimpton, Fast Parallel Algorithms for Short-Range Molecular Dynamics, *J. Comput. Phys*., 1995, 117, 1-19.

(S14)A. P. Thompson, H. M. Aktulga, R. Berger, D. S. Bolintineanu, W. M. Brown, P. S. Crozier, P. J. in 't Veld, A. Kohlmeyer, S. G. Moore, T. D. Nguyen, R. Shan, M. J. Stevens, J. Tranchida, C. Trott, S. J. Plimpton, LAMMPS - a flexible simulation tool for particle-based materials modeling at the atomic, meso, and continuum scales, *Comput. Phys. Commun*., **2022**, *271*, 108171.

(S15) D. H. Lu, W. R. Jiang, Y. X. Chen, L. F. Zhang, W. L. Jia, H. Wang, M. H. Chen, DP Compress: A Model Compression Scheme for Generating Efficient Deep Potential Models, *J. Chem. Theory Comput.*, **2022**, *18*, 5559-5567.

(S16) N. Michaud-Agrawal, E. J. Denning, T. B. Woolf, O. Beckstein, MDAnalysis: A toolkit for the analysis of molecular dynamics simulations, *J. Comput. Chem*., **2011**, *32*, 2319-2327.